RSC Advances

PAPER

Cite this: *RSC Adv.*, 2019, **9**, 42010

Novel lanthanide(III) 4-methylbenzoylhydrazide complexes as precursors for lanthanide oxide nanophotocatalysts

S. A. Abou El-Enein, *[a] A. M. Ali,[a] Y. K. Abdel-Monem,[a] M. H. Senna[b] and Metwally Madkour *[c]

A series of metal complexes were prepared from separate reactions of lanthanide nitrate salts (La(III), Ce(III), Sm(III), Gd(III) and Ho(III)) with 4-methylbenzoylhydrazide. The structures of the complexes were confirmed by analytical studies, spectral measurements and thermal studies. Complexes were formed with different stoichiometries of 1 : 2 and 1 : 3 (M : L). The ligand chelates by the nitrogen and oxygen atoms of the amino and carbonyl groups of the hydrazide moiety in the neutral keto form. The coordination compounds were converted to metal oxide nanoparticles (MONPs) through solid state thermal decomposition as monocular source precursors. The obtained MONPs were investigated *via* XRD, TEM and UV-Vis spectra. As a representative, CeO_2 was utilized as a nanophotocatalyst to examine the photocatalytic activity of the MONPs for methylene blue (MB) photodegradation. CeO_2 showed high removal of MB dye by 90.1% after UV illumination for 220 min. The reported method provides a generalized and systematic method for the preparation of many metal oxide nanoparticles with manageable and reproducible features.

Received 5th October 2019
Accepted 14th November 2019

DOI: 10.1039/c9ra08080e

rsc.li/rsc-advances

1. Introduction

Hydrazide compounds contain terminal NH_2 groups and are precursors for numerous synthesized Schiff and azo compounds. Hydrazides and their derivatives have potential active sites; C=O, NH and NH_2 have the ability to coordinate with different metal ions.[1] Hydrazides and their derivative metal complexes have applications in biological fields as insecticidal, acaricidal, nematicidal, and antileishmanial agents and inhibit protease enzymes in some parasitic species and diamine oxidases.[1] Their lanthanide complexes have luminescent and magnetic properties; thus, they can be used in electroluminescent devices.[2,3] Also, due to their exhibited spectroscopic, magnetic, and chemical properties, these lanthanide complexes have many useful applications compared to other metal complexes. This is due to the fluxional nature of lanthanide(III) ion, which possesses high and variable coordination numbers as well as a lack of angular preference.[4] Hydrazide lanthanide complexes are an ongoing area of active research due to their good antioxidant activities and their biological activities, such as anticoagulation, antiallergic, antibacterial, anti-inflammatory and anticancer. Also, they have been used for treatment of burns.[5–7]

Metal oxide nanoparticles show a wide range of applications, including catalysis, sensing, optics, semiconductors, solar cells, batteries and biotechnology. Also, metal oxide nanoparticles have been used as nanophotocatalysts for the degradation of methylene blue and Safranin-O dyes.[8–12] The synthesis of metal oxide nanoparticles from their corresponding metal complexes is of great interest. This technique offers several unique advantages over other methods, including facility, reproducibility, short reaction times, short washing and drying durations, and production of inorganic nanomaterials with narrow size distributions.[9]

In this work, we aimed to synthesize lanthanide metal complexes of lanthanum(III), cerium(III), samarium(III), gadolinium(III), and holmium(III) with 4-methylbenzoylhydrazide ligand. Structural characterization of all the prepared compounds was performed based on elemental analysis, spectral methods (UV-Vis, IR, ^{1}H NMR, and mass spectroscopy), molar electrical conductivity, magnetic susceptibility and thermal analyses. Also, nano-metal oxides were prepared by thermal degradation of the metal complexes, and their applications in wastewater treatment were studied through photocatalytic degradation of methylene blue.

2. Experimental

2.1 Materials and methods

All chemicals were of analytical grade (BDH, Sigma or Aldrich) and were used as received without further purification.

[a]Department of Chemistry, Faculty of Science, Menoufia University, Shibin El Kom, Egypt. E-mail: dr.saeyda_elenein@yahoo.com
[b]Radiation Chemistry Department, National Center for Radiation Research and Technology, Cairo, Egypt
[c]Department of Chemistry, Faculty of Science, Kuwait University, P. O. Box: 5969, 13060, Kuwait. E-mail: metwally.madkour@ku.edu.kw

Elemental microanalysis (C, H, and N) was performed using a PerkinElmer-2400 elemental analyzer at Main Defense Chemical Laboratory. Infrared spectra were registered on a JASCO FTIR-6300 spectrophotometer in the range of 4000 to 400 cm^{-1} to investigate the infrared spectral bands. The ^{1}H-NMR spectra were recorded in DMSO-d_6 on a Bruker NMR spectrometer at 600 MHz. Fast atom bombardment (FAB) mass spectra for the ligand and its La(III) and Gd(III) complexes were acquired using a spectrometer. The electronic absorption spectral bands were revealed in Nujol mulls using Varian Vary 5000 UV-Vis spectrophotometer. Molar conductance measurements of the complexes in 10^{-3} M DMSO were performed using a Tacussel CD6N conductimeter. The magnetic susceptibility was measured at room temperature by a modified Gouy method using a Johnson Mathey magnetic susceptibility balance. A Shimadzu DAT/TG-50 thermal analyzer was used to conduct the thermogravimetric analysis (TG and DTG) under certain conditions (a heating rate of 10 °C min^{-1} under nitrogen and oxygen atmosphere with a flowing rate of 20 ml min^{-1} from room temperature to 900 °C using platinum crucibles). Melting points were detected by a Stuart melting point apparatus. The X-ray diffraction (XRD) measurements for the MONPs were performed using an Bruker D8 Advance diffractometer with a copper target and nickel filter with CuKα radiation (k = 0.154056 nm). Measurements were performed in the 2θ range of 20° to 80°. The morphology of the CeO_2 nanoparticles was obtained by transmission electron microscopy (TEM) with a JEOL JEM 1230 (JEOL Ltd., Japan) operating at 120 kV. The average particle size was determined statistically by manually counting 90 particles.

2.2 Synthesis of 4-methylbenzoylhydrazide ligand (HL)

The ligand was prepared as reported.[13] The reaction was performed by dissolving 4-toulic acid in ethanol in the presence of conc. sulfuric acid as a catalyst to yield the ester derivative. Then, an excess of hydrazine hydrate was added. The reaction mixture was refluxed for 4 h. The solid ligand was filtered, washed, and recrystallized from methanol to afford pale yellow crystals which were finally dried under vacuum over anhydrous calcium chloride. The measured melting point was 164 °C.

2.3 Synthesis of the lanthanide(III) complexes

The complexes were synthesized by adding an appropriate ethanolic solution of $M(NO_3)_3 \cdot nH_2O$ (M = La(III), Ce(III), Sm(III), Gd(III) and Ho(III), n = 3 to 6) to an ethanolic solution of ligand with a molar ratio of 1 : 3 (M : L). The mixture was stirred for three hours at 50 °C, then filtered, washed and completely dried under vacuum over anhydrous $CaCl_2$.

2.4 Preparation of metal oxide nanoparticles

In a typical procedure, certain amounts of La(III), Ce(III), Sm(III), Gd(III) and Ho(III) complexes were maintained inside a crucible and heated to 600 °C under air in a muffle furnace for 60 minutes (heating rate: 10 °C min^{-1}). The thermal degradation of the coordinated precursors resulted in the formation of their analogue metal oxides. The produced oxides were cooled to room temperature and then collected for analysis.

2.5 Photocatalytic activity

The photodegradation test for methylene blue dye (model pollutant) was performed as follows: CeO_2 nanoparticles (10 mg/100 ml) were dispersed in methylene blue aqueous solution (10 ppm) using a sonicator for 20 minutes in the dark to exclude the adsorption results. After that, the solution was irradiated with a UV lamp (6 W at a wavelength of 254 nm). Aliquots of 5.0 ml of the tested solution were collected each 20 min, centrifuged at 5000 rpm to monitor absorbance changes, then analyzed spectrophotometrically to detect the absorbance changes as a function of irradiation time.

3. Results and discussion

3.1 Analytical data

Table 1 presents the analytical data of the prepared lanthanide(III) nitrate complexes. The prepared complexes have the chemical formulas $[La(HL)_2(NO_3)_2]\cdot NO_3 \cdot EtOH$, $[Ce(HL)_3(NO_3)_2]\cdot$

Table 1 Analytical data and molar conductance values of 4-methylbenzoylhydrazide (HL) and its metal complexes

			Elemental analysis, F (cal.)%				
No.	Compound	Colour, F. W.	C	H	N	Mp	A^a
	$HL^1 \cdot 0.5H_2O$, $C_8H_{11}N_2O_{1.5}$	Off-white, 159.19	60.67, (60.36)	6.42, (6.96)	17.64, 17.59	132	—
1	$[La(HL)_2(NO_3)_3]\cdot EtOH$, $C_{18}H_{26}N_7O_9La$	White, 623.35	34.49, (34.40)	3.67, (3.95)	15.05, (14.78)	222	42
2	$[Ce(HL)_3(NO_3)_2]\cdot NO_3$, $C_{24}H_{30}N_9O_{12}Ce$	White, 812.67	36.96, (37.11)	3.94, (3.89)	16.22, (16.23)	238	52
3	$[Sm(HL)_3(NO_3)_2]\cdot NO_3 \cdot H_2O$, $C_{24}H_{32}N_9O_{13}Sm$	White, 804.93	35.66, (35.81)	4.00, (4.01)	16.09, (15.67)	246	56
4	$[Gd(HL)_3(NO_3)_2]\cdot NO_3 \cdot 0.5H_2O$, $C_{24}H_{31}N_9O_{12.5}Gd$	White, 802.81	36.06, (35.91)	3.82, (3.89)	15.69, (15.75)	248	55
5	$[Ho(HL)_3(NO_3)_2]\cdot NO_3 \cdot 0.5EtOH$, $C_{25}H_{32}N_9O_{12.5}Ho$	White, 854.52	35.99, (35.13)	3.82, (3.77)	15.68, (14.75)	250	54

^{a} (Ω^{-1} cm^2 mol^{-1}).

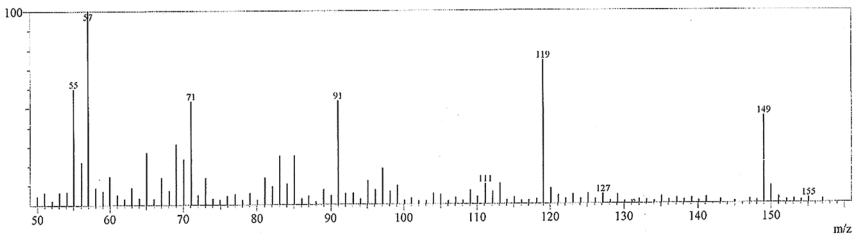

Fig. 1 FAB mass spectrum of the ligand.

NO_3, $[Sm(HL)_3(NO_3)_2]\cdot NO_3\cdot H_2O$, $[Gd(HL)_3(NO_3)_2]\cdot NO_3\cdot 0.5H_2O$ and $[Ho(HL)_3(NO_3)_2]\cdot NO_3\cdot 0.5EtOH$. The complexes are stable in air and non-hydroscopic. All the chelates showed solubility in polar and nonpolar solvents. The molar conductance values of the complexes were in the range of 52 to 56 Ω^{-1} cm^2 mol^{-1}, which demonstrates the uni-electrolytic properties of all the complexes.[14]

3.2 Spectral studies

3.2.1 Mass spectra. The FAB mass spectra of the ligand is shown in Fig. 1. The FAB mass spectrum of the hydrazide ligand (Fig. 1) contains a molecular ion peak at *m*/*z* 150.0 amu, which matches the theoretical molecular weight of the ligand without solvent. This proved its formation. Also, the spectrum exhibited other degradation peaks at 119, 91.05, 76, and 55 amu, which are assignable to $[C_8H_7O]^+$, $[C_7H_7]^+$, $[C_6H_4]^+$ and 4.5C, respectively; this is compatible with Scheme 1. The mass spectra of the La(III) and Gd(III) complexes are consistent with the formulae $[La(HL)_2(NO_3)_3]\cdot$EtOH and $[Gd(HL)_3(NO_3)_2]\cdot NO_3\cdot 0.5H_2O$, giving parent molecular ions at *m*/*z* 623 and 803, respectively; this confirms the theoretical data.

3.2.2 ^{1}H-NMR. The ^{1}H-NMR spectrum of the ligand (HL) and its lanthanum(III) complex are compiled in Table 2 and represented in Fig. 2. The spectrum of the ligand exhibits signals at δ, ppm: 2.32 (3H, s, CH_3), 4.52 (2H, s, NH_2), 7.22 to 7.82 (4H, s, Ar-CH) and 9.69 (1H, s, NH).[15,16] In comparison, the spectrum of the La(III) complex shows signals at 2.92, 4.80, and 9.77 ppm, which are assigned to CH_3, NH_2, and NH,

Table 2 ^{1}H NMR spectra of hydrazide ligand (HL) and its La(III) complex

(HL)	La(III) complex	Assignment
2.32	2.33–2.49	3H of 2(CH_3)
4.52	4.80	2H of (NH_2)
7.22–7.82	7.23–7.72	H of (CH)
9.69	9.77	1H of (NH)

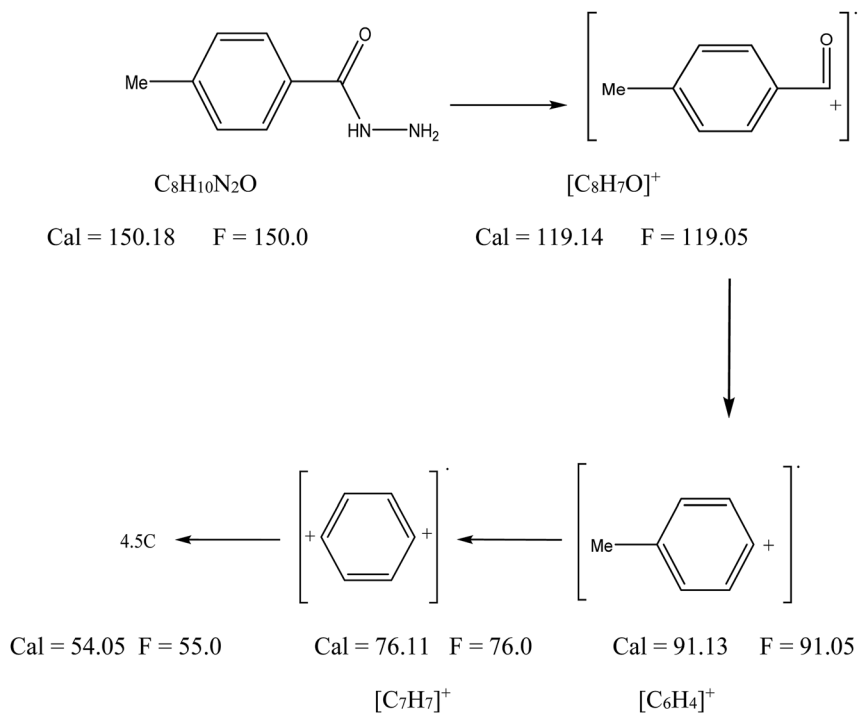

Scheme 1 Mass ion of the HL ligand and its fragmentation.

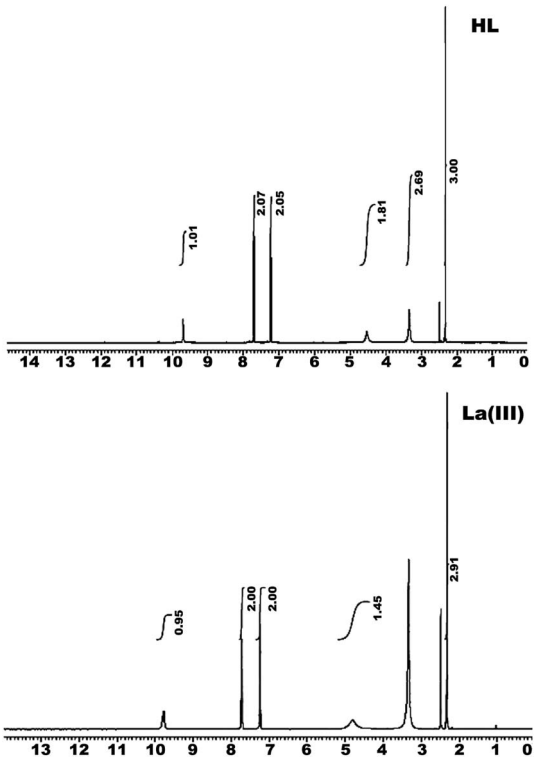

Fig. 2 ^{1}H NMR spectra of the hydrazide ligand (HL) and its La(III) complex.

respectively. The NH_2 signal shifted downfield relative to the uncoordinated ligand, confirming its involvement in chelation. The absence of a signal at 12 to 14 ppm assigned to the enolic OH suggests that the ligand chelated with metal ion in its neutral keto structure.

3.2.3 Infrared spectra of the ligand (HL) and its metal complexes. The fundamental spectral bands and their assignments of the ligand and its metal complexes are tabulated in Table 3 and diagrammed in Fig. 3. The spectrum of the ligand contains strong bands at 3306, 3222, 3027, 1616, and 1503 cm^{-1}; 1042 and 922 cm^{-1}; and 787, 719 and 446 cm^{-1}, which can be assigned to $\upsilon_{asy}(NH_2)$, $\upsilon_{sy}(NH_2)$, υ(NH), $\delta(NH_2)$, and $\delta(NH)_{amide}$; υ(N–N), $\gamma(NH_2)$, and $\gamma(NH)_{amide}$; and $\rho(NH_2)$, respectively.[16] The carbonyl groups are assigned to strong bands located at 1659 and 677 cm^{-1}, 633 cm^{-1} and 522 cm^{-1}, attributed to υ(C=O), δ(C=O), and γ(C=O), respectively. The spectrum of the ligand exhibits the presence of fundamental bands corresponding to NH and C=O (υ, δ, γ) with the absence of υ(OH); this indicates that the ligand has a keto structure. The spectrum of the ligand shows additional fundamental bands at 2920 and 2878 cm^{-1} due to the υ(CH) aromatic and methyl groups, respectively. Comparison of the spectral bands of the ligand with those of its metal complexes led to the following observations: υ_{asy}, υ_{sy}, and δ of the NH_2 and υ(C=O) groups of the ligand undergo blue shifts at 10 to 13 cm^{-1} upon complexation. However, δ(C=O) of the ligand at 617 cm^{-1} disappeared, while the second one at 633 cm^{-1} shifted to lower values by 5 to 17 cm^{-1} upon complexation.

Table 3 Infrared spectral bands (cm^{-1}) and their assignments for hydrazide ligand (HL) and its metal complexes[a]

No.	Compound	υ_{as} (NH_2)	υ_{sy} (NH_2), $\gamma(NH_2)$	υ_{amide} (NH), γ(NH)	υ(C=O)	$\delta(NH_2)$	υ(N–N)	δ(C=O), γ(C=O)	γ(C=O), υ(M–O)	$\rho(NH_2)$, υ(M–N)	NO_3^- band		
											Ionic	υ_4	υ_1
	(HL)0.5H_2O	3306(s)	3222(s), 787(w)	3027(s), 719(s)	1659(s)	1616(s)	1042(w), 992(s)	677(m), 633(s)	522	446(m)			
1	[La(HL)$_2$(NO_3)$_3$]·EtOH	3295(m)	3216(m), 792(vw)	3060(vw), 778(w)	1647(m)	1603(m)	1034(vw), —	—, 6159(w)	516	—	1384	1466	1210
2	[Ce(HL)$_3$(NO_3)$_2$]·NO_3	3295(b, m)	3210(w), 792(w)	3022(w), 778(w)	1648(m)	1605(m)	1034(vw), —	613(w)	518	462(w)	1384	1464	1208
3	[Sm(HL)$_3$(NO_3)$_2$]·NO_3·H_2O	3295(w)	3207(w), 792(vw)	—, 748(w)	1648(s)	1603(sh)	1037(vw), —	—, 621(m)	528	463(w)	1382	1465	1212
4	[Gd(HL)$_3$(NO_3)$_2$]·NO_3·0.5H_2O	3297(w)	3210(w), —	—, 748(w)	1646(s)	1606(s)	1038(vw), —	—, 630(m)	527	472(w)	1383	1465	1212
5	[Ho(HL)$_3$(NO_3)$_2$]·NO_3·0.5EtOH	3297(m)	3208(m), 794(vw)	—, 748(m)	1649(s)	1606(w)	1038(w)	—, 628(m)	528	463(w)	1383	1463	1210

[a] vw: very weak, w: weak, m: medium, s: strong, b: broad, sh: shoulder.

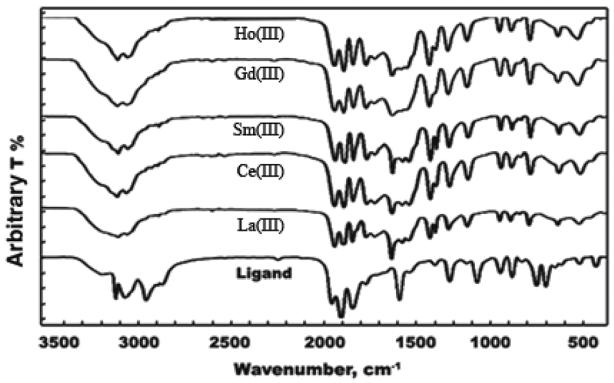

Fig. 3 IR spectra of the ligand and its metal complexes.

The above assignments indicate that the metal ions attach to the ligand *via* carbonyl oxygen and amino nitrogen atoms, leading to the construction of five-membered rings. The ligand bands at 522 and 446 cm^{-1} due to γ(C=O) and $\rho(NH_2)$ exhibit shifts in the ranges of 518 to 528 and 462 to 472 cm^{-1} upon complexation, which are attributed to υ(M–O) and υ(M–N), respectively.[17] The absorption bands appearing at around 1380 and 784 cm^{-1} in the spectra of the investigated complexes are assigned to the ionic nitrate group.[14] The complexes exhibit absorption bands in the regions of 1463 to 1466 cm^{-1} and 1208 to 1212 cm^{-1}; these are not observed in the spectrum of the ligand and can be assigned to υ_4 and υ_1, respectively. This situation suggests that the nitrate ions are covalently bonded and are located in the coordination sphere; this indicates that the magnitude of separation $\Delta\upsilon = \upsilon_1 - \upsilon_4$ is sufficiently greater than 200 cm^{-1}, considering that the nitrate groups are covalently bonded to the metal ion in bidentate fashion. The data show that the lanthanide nitrate complexes contain both coordinated and ionic nitrate groups, which confirms the chemical formulae.

Table 4 Electronic absorption spectra and magnetic moment values of the ligand and its complexes

No.	Compound	Electronic spectral bands (nm)	Assignment	μ/μ_B
	$(HL)0.5H_2O$	296, 272, 240	N–π*, π–π*	—
1	$[La(HL)_2(NO_3)_3]\cdot EtOH$	308, 284, 242	n–π*, π–π*	Diam
2	$[Ce(HL)_3(NO_3)_2]\cdot NO_3$	297, 287, 242	n–π*, π–π*	3.09
3	$[Sm(HL)_3(NO_3)_2]\cdot NO_3\cdot H_2O$	313, 284, 242	n–π*, π–π*	3.69
4	$[Gd(HL)_3(NO_3)_2]\cdot NO_3\cdot 0.5H_2O$	312, 284, 246	n–π*, π–π*	7.91
5	$[Ho(HL)_3(NO_3)_2]\cdot NO_3\cdot 0.5EtOH$	312, 284, 242	n–π*, π–π*	10.78

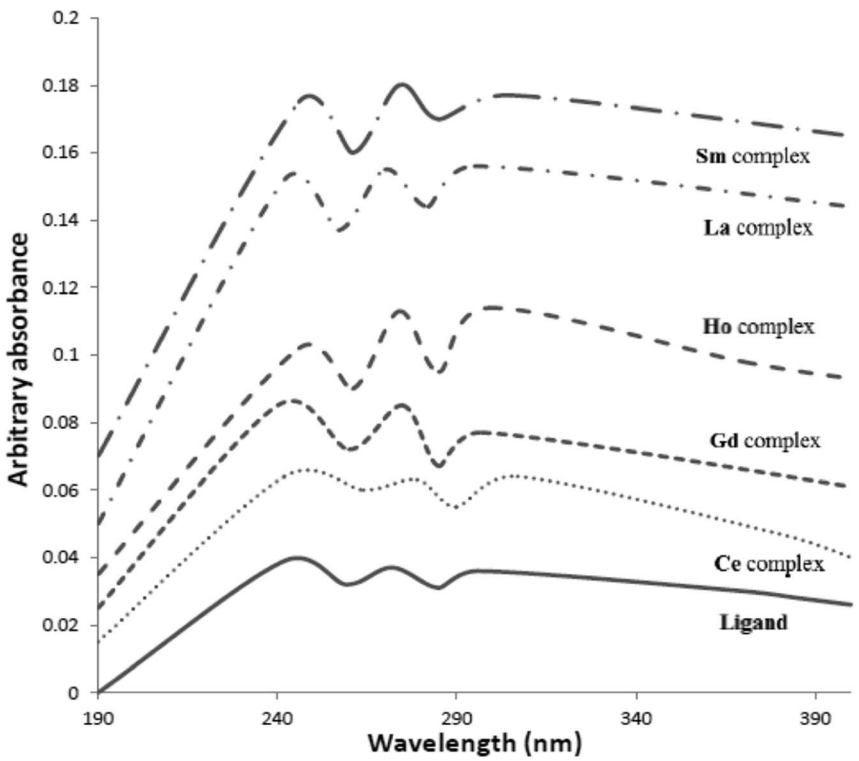

Fig. 4 Electronic absorption spectra of the ligand and its complexes.

Table 5 Thermal decomposition of the ligand and its metal complexes

No.	Compound	TG range (°C)	DTA peak (°C)	Mass loss% found (calcd.)	Assignment	TS (°C)
1	$(HL)\cdot 0.5H_2O$	109–163		2.70 (2.83)	Loss of 0.25 mol of H_2O[a]	163
		163–292		69.37 (70.14)	Ligand pyrolysis[c]	
		292–322		26.13 (24.52)	Complete ligand pyrolysis[c]	
2	$[La(HL)_2(NO_3)_3]\cdot EtOH$	30–228		7.39 (8.18)	Loss of 1 mol of EtOH[b]	228
		228–325	293	55.21 (55.90)	Loss of 1 mol of L + 2 mol of NO_3^- + 1 mol of NO_2[c]	
		325–787	487	18.95 (17.73)	Complete ligand pyrolysis[c]	
		At 787		18.44 (18.91)	$0.5La_2O_3$[d]	
3	$[Ce(HL)_3(NO_3)_2]\cdot NO_3$	30–206		7.49 (7.63)	Loss of 1 mol of NO_3^-[b]	206
		206–250	231	63.80 (63.56)	Loss of 2 mol of L + 2 mol of NO_3^-[c]	
		250–466	387	7.06 (6.89)	Complete L pyrolysis[c]	
		At 466		20.65 (20.19)	$0.5Ce_2O_3$[d]	
4	$[Sm(HL)_3(NO_3)_2]\cdot NO_3\cdot H_2O$	30–217		2.60 (2.24)	Loss of 1 mol of H_2O[a]	217
		217–297	257	56.93 (58.43)	Loss of 2 mol of L + 2 mol of NO_3^- + 1 mol of NO_2[c]	
		297–692	467	19.34 (17.92)	Complete ligand pyrolysis[c]	
		At 692		21.41 (21.67)	$0.5Sm_2O_3$[d]	
5	$[Gd(HL)_3(NO_3)_2]\cdot NO_3\cdot 0.5H_2O$	30–267		1.36 (1.12)	Loss of 0.5 mol of H_2O[a]	267
		267–334	290	64.81 (65.07)	Loss of 2 mol of L + 1 mol of NO_3^- + 1 mol of NO_2	
		334–893	453	11.55 (11.23)	Complete ligand pyrolysis[c]	
		At 893		22.41 (22.58)	$0.5Gd_2O_3$[d]	
6	$[Ho(HL)_3(NO_3)_2]\cdot NO_3\cdot 0.5EtOH$	30–234		2.70 (2.81)	Loss of 0.5EtOH[b]	234
		234–300	174	64.42 (63.89)	Loss of 2 mol of L + 2 mol of NO_3^- + 1 mol of NO_2[c]	
		300–575	264	11.01 (11.23)	Complete ligand pyrolysis[c]	
		At 575	452	22.11 (22.08)	$0.5Ho_2O_3$[d]	

[a] Dehydration. [b] Desolvation. [c] Decomposition. [d] Remain.

3.2.4 Electronic absorption spectra. The electronic spectral data of the hydrazide organic compound (HL) and its metal chelates in Nujol mulls are reported in Table 4 and demonstrated in Fig. 4. The electronic spectrum of the ligand displays spectral bands in the range of 272 to 240 nm and at 296 nm, assigned to the π–π* and n–π* electronic transitions of the entire conjugate system of the ligand, respectively. On the other hand, the electronic spectra of the metal chelates (1–5) display π–π* and n–π* transitions of the ligand, which are shifted to higher values upon complexation; this indicates that chelation was achieved. None of the spectra of the complexes showed bands in the visible region. This is probably due the fact that the f–f bands are weak and obscured by the intense charge transfer bands.[18,19] The magnetic moments of the lanthanide(III) complexes indicate that only the La(III) complex is diamagnetic, and the other tripositive lanthanide ion complexes are paramagnetic.

3.2.5 Thermal analysis of the metal complexes. The thermograms (TG, DTA) gathered with thermoanalytical data and their assignments for each decomposition step to follow the decomposition pathways for the ligand and its metal complexes are given in Table 5 and Fig. 5. The TGA curve of the ligand shows thermal stability up to 109 °C followed by a small weight loss of 2.70% up to 163 °C, corresponding to the release of 0.25 mol of H_2O. The pyrolytic process was achieved through two steps by TG weight losses of 69.37% and 26.13% and DTA peaks at T_{max} = 180 °C and 292 °C, respectively. The DTA curve displays a sharp endothermic peak at 132 °C, which is assignable to the melting point of the compound and corresponds with the measured value. The thermoanalytical data in Table 5 combined with the TG and DTA patterns of the La(III), Sm(III), Gd(III), and Ho(III) complexes show that these complexes decompose in a similar way, indicating that they are isothermal.

The TG curves showed weight losses in the temperature range of 30 °C to 234 °C due to removal of the solvents of crystallization. After that, the chelates decomposed in two consecutive stages. The first stage exhibited weight losses of 55.21%, 56.90%, 64.80% and 64.42% from 228 °C to 325 °C, 217 °C to 297 °C, 214 °C to 334 °C and 234 °C to 300 °C for La(III), Sm(III), Gd(III) and Ho(III), respectively. This process is associated with sharp exothermic DTA peaks at T_{max} = 293 °C, 257 °C, 290 °C, and 264 °C, respectively; this signifies that the oxidative process of the ligand involves the release of two moles of organic ligand (one mole in the La(III) complex), two moles of NO_3 groups and one mole of NO_2 gas. The last ligand pyrolysis was characterized by TG weight losses of 18.93%, 19.34%, 11.55% and 11.01% up to 787 °C, 692 °C, 893 °C and 575 °C for the La(III), Sm(III), Gd(III) and Ho(III) complexes, respectively. The thermal decomposition process ended with the formation of 0.5 M_2O_3 (M = La(III), Sm(III), Gd(III) and Ho(III)). However, the TG curves of the Ce(III) complex reveal a weight loss of 7.49% in the 30 °C to 206 °C range due to elimination of the ionic nitrate group. This step was followed by a TG weight loss of 63.8% up to 250 °C. This process was accompanied by two exothermic DTA peaks at T_{max} = 231 °C to 253 °C, indicating the oxidation of the ligands with removal of two moles of the ligand and two

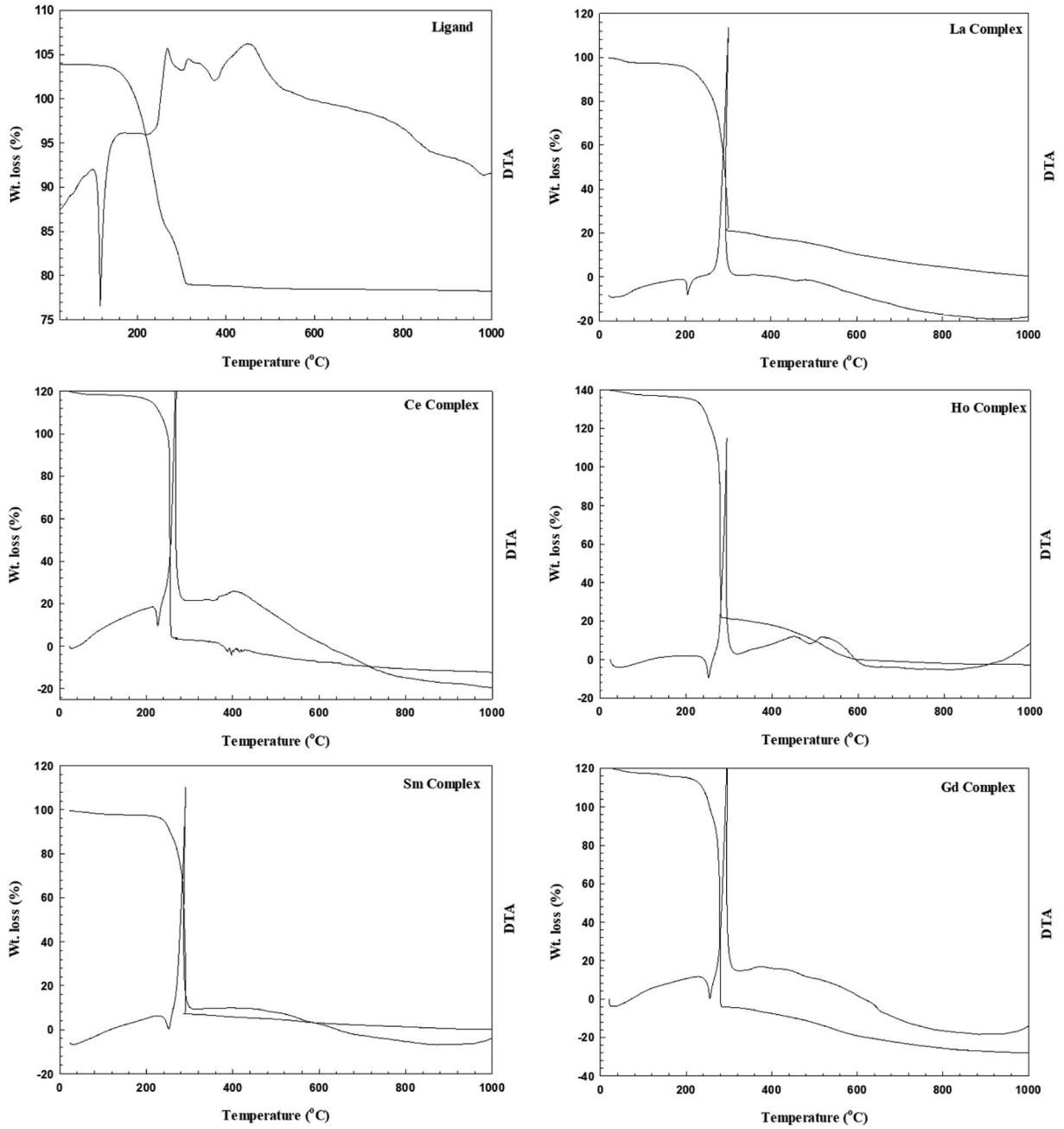

Fig. 5 Thermograms of the ligand and its metal complexes.

moles of the coordinated nitrate group. The last decomposition step exerted a TG weight loss of 6.89% in the 250 °C to 466 °C range due to complete ligand pyrolysis, and the metal reacts with atmospheric oxygen to produce $0.5Ce_2O_3$ as a product. This process is associated with the exothermic DTA peak at $T_{max} = 387$ °C.

3.3 Characterization of nanoparticles

In Fig. 6, the diffraction peaks for CeO_2 at 28.5°, 33.0°, 47.4° and 56.3° can be indexed to the (111), (200), (220) and (311) planes of the face-centered cubic structure of CeO_2 (JCPDS no. 81-0792). For the La_2O_3 NPs, the peaks obtained at 28.67°, 31.21°, 43.28°, 47.86°, 59.29°, 64.97° and 70.12° are indexed to the (002), (400), (125), (600), (127), (800) and (822) planes, respectively, and assigned as per JCPDS no. 65-3185.[20] For the Sm_2O_3 NPs, the diffraction peaks located at 28.2°, 32.7°, 38.6°, 45.4°, and 54.3° correspond to the (222), (400), (332), (521), and (541) planes of cubic Sm_2O_3 (JCPDS no. 15-0813), respectively.[21] For the Ho_2O_3 NPs, diffraction lines of cubic holmium oxide (JCPDS card 88-2163) were obtained.[22] For the Gd_2O_3 NPs, the pattern was well-indexed with the cubic structure reported in the standard JCPDS card no. 43-1014.[23] No diffraction peaks of any impurity were observed, indicating the high purity of the final products. These results

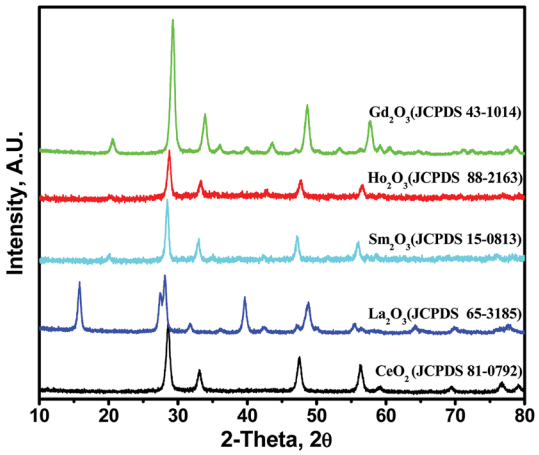

Fig. 6 X-ray diffraction patterns of the prepared lanthanide oxide nanoparticles.

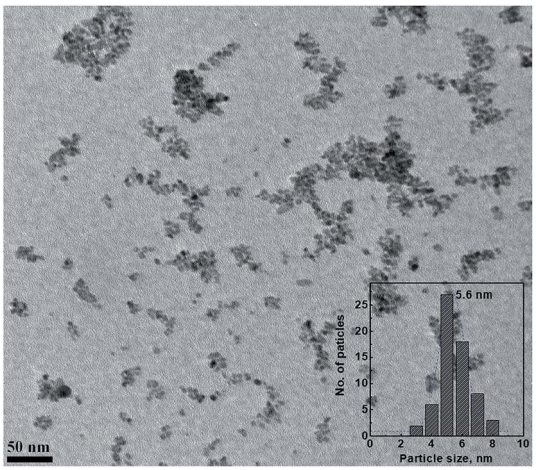

Fig. 8 TEM image of the CeO_2 nanoparticles. The inset is the size distribution for CeO_2 nanoparticles.

suggest that the precursor samples crystallized into their analogous oxide nanoparticles at a heating temperature of 700 °C. The crystallite sizes for the lanthanide oxide NPs were calculated using the Debye–Scherrer equation:[24]

$$D = k\lambda/(\beta \cos \theta) \quad (1)$$

where k is a shape factor ($k = 0.89$), λ is the wavelength of the radiation, β is the full width at half maximum (FWHM) and θ is the angle corresponding to the most intense peak in the XRD pattern. The crystallite sizes were found to be 2.9 nm, 3.7 nm, 4.2 nm, 3.8 nm and 3.3 nm for the CeO_2, La_2O_3, Sm_2O_3, Ho_2O_3 and Gd_2O_3 NPs, respectively.

The absorption spectra for the prepared lanthanide oxide nanoparticles were measured, as shown in Fig. 7. All the nanoparticles showed similar absorption behavior, with a strong absorption peak at ~240 to 250 nm, which is consistent with the literature. The band gap energy values for the lanthanide oxide nanoparticles were calculated using Tauc plots by applying the equation $(\alpha h\nu)^{1/n} = A(h\nu - E_g)$,

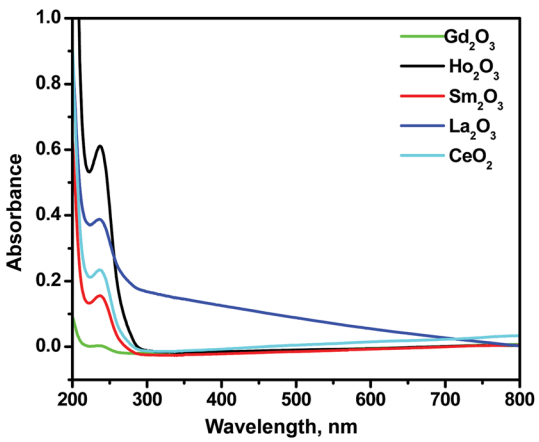

Fig. 7 UV-Vis absorption spectra of the prepared lanthanide oxide nanoparticles.

where h is Planck's constant, ν is the photon frequency, α is the absorption coefficient, E_g is the band gap, the exponent n denotes the nature of the electronic transition (direct or indirect), and A is a proportionality constant. The calculated values were found to be in the range of 4.64 to 4.85 eV. The increase of the band gap can be attributed to the quantum confinement effect, which led to decreased charge carrier recombination rates.[20] The sizes and morphologies of the CeO_2 nanoparticles were investigated by TEM. The TEM image of CeO_2 is shown in Fig. 8. From the figure, the nanoparticles can be found to be monodisperse and spherical, with an average particle size of 5.6 nm.

3.4 Photocatalytic activity

Because all the prepared NPs revealed the same absorption spectra and band gap energy values, in this work, the CeO_2 NPs were chosen for evaluation as a photocatalyst due to their smaller particle size relative to the other metal oxides. Photocatalytic degradation of MB dye using the CeO_2 NPs as a model photocatalyst was performed to evaluate their photocatalytic activity. Fig. 9 shows the photocatalytic activity of the CeO_2 NPs. The photo degradation efficiency was calculated to be 90.1%, as shown in Fig. 9B. Fig. 9C showed that the photodegradation reaction follows pseudo-first-order kinetics. The photodegradation rate constant for the photodegradation reaction was determined from the equation:

$$\ln(C_o/C) = kt \quad (2)$$

where C_o and C are the initial concentration and the concentration at time t, respectively, and k is the apparent first-order rate constant. The plot of $\ln(C_o/C)$ *versus* time represents a straight line, as shown in Fig. 9C; the slope upon linear regression equals the apparent first-order rate constant k. The degradation rate obtained was 0.014 min^{-1}. To evaluate the photostability of CeO_2, four photodegradation experiments (reusability tests) under identical conditions were performed.

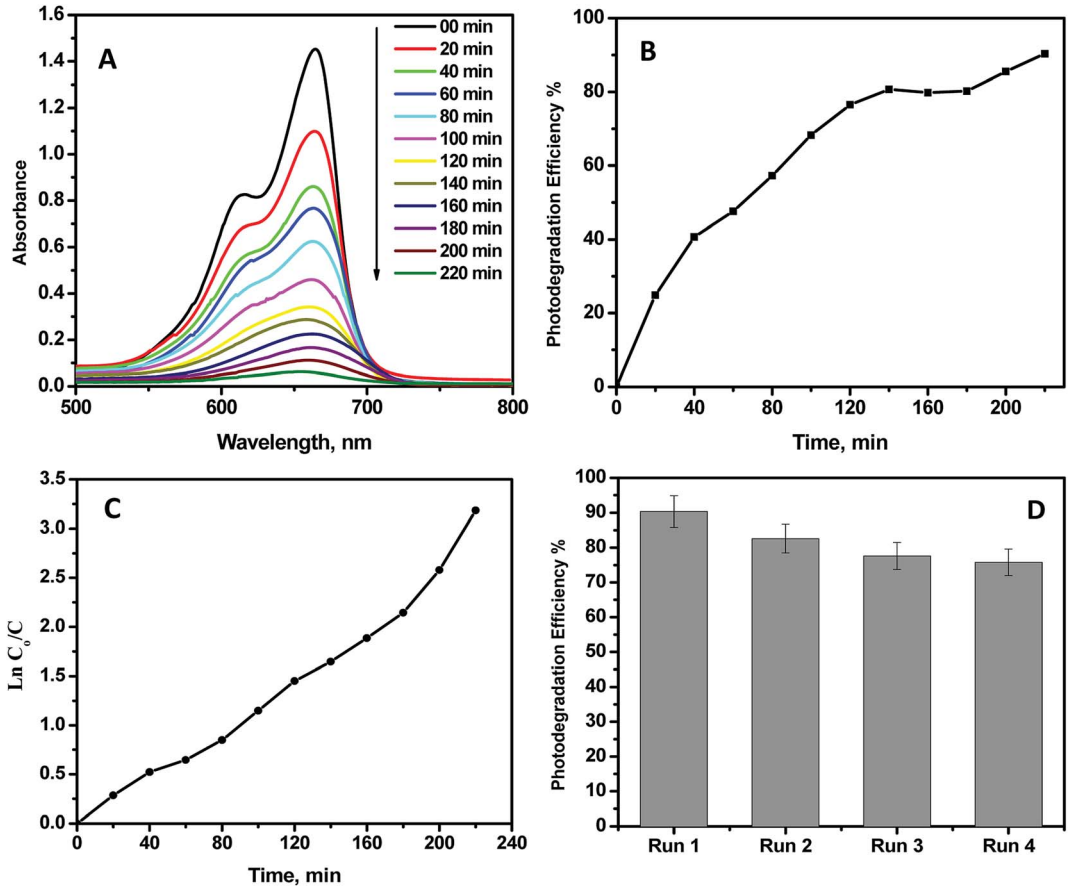

Fig. 9 (A) Methylene blue dye absorption spectra at different times upon irradiation with CeO_2. (B) Evaluation of MB conversion efficiency upon irradiation. (C) Kinetics of MB photocatalytic degradation. (D) Reusability of CeO_2 nanoparticles.

From Fig. 9D, it can be noted that CeO_2 was almost completely stable and photoactive up to the 4th run, as its photocatalytic activity decreased by only 15% after the 4th run.

4. Conclusion

In this work, a series of metal complexes were prepared by separate reactions of lanthanide nitrate salts (La(III), Ce(III), Sm(III), Gd(III) and Ho(III)) with 4-methylbenzoylhydrazide. The structures of the complexes were confirmed by analytical studies, different spectral measurements and thermal studies. Complexes were formed with different stoichiometries of 1 : 2 and 1 : 3 (M : L). The coordination compounds were converted to metal oxide nanoparticles (MONPs) through solid state thermal decomposition as monocular source precursors. The obtained MONPs were investigated *via* XRD, TEM and UV-Vis spectral analyses. CeO_2 was utilized as a representative nano-photocatalyst to examine the photocatalytic activity of the MONPs in methylene blue (MB) photodegradation. The CeO_2 catalyst showed high MB removal of 90.1% after UV illumination for 220 min. The reported method provides a generalized and systematic method for the preparation of many nanoparticle metal oxides with manageable and reproducible features.

Conflicts of interest

There are no conflicts to declare.

Acknowledgements

The authors gratefully acknowledge RSPU at Kuwait University, Facilities No. GS 01/01, GS 01/03, GS 01/05, GS 02/01, GS 02/08, GS 03/01 and GE 03/08. The Nanoscopy Science Center is also highly acknowledged.

References

1 S. A. Galal, K. H. Hegab, A. S. Kassab, M. L. Rodriguez, S. M. Kerwin, A.-M. m. A. El-Khamry and H. I. El Diwani, *Eur. J. Med. Chem.*, 2009, **44**, 1500–1508.
2 J.-C. G. Bünzli and S. V. Eliseeva, *J. Rare Earths*, 2010, **28**, 824–842.
3 J.-C. G. Bünzli, *Chem. Rev.*, 2010, **110**, 2729–2755.
4 P. Starynowicz and J. Lisowski, *Polyhedron*, 2015, **85**, 232–238.
5 Q.-L. Guan, Y.-H. Xing, J. Liu, W.-J. Wei, R. Zhang, X. Wang and F.-Y. Bai, *J. Inorg. Biochem.*, 2013, **128**, 57–67.

6 M. Albrecht, O. Osetska and R. Fröhlich, *Dalton Trans.*, 2005, 3757–3762.
7 R. Wai-Yin Sun, D.-L. Ma, E. L.-M. Wong and C.-M. Che, *Dalton Trans.*, 2007, 4884–4892.
8 M. Madkour, Y. K. Abdel-Monem and F. Al Sagheer, *Ind. Eng. Chem. Res.*, 2016, **55**, 12733–12741.
9 Y. K. Abdel-Monem, S. M. Emam and H. M. Y. Okda, *J. Mater. Sci.: Mater. Electron.*, 2017, **28**, 2923–2934.
10 Y. K. Abdel-Monem, *J. Mater. Sci.: Mater. Electron.*, 2016, **27**, 5723–5728.
11 A. Bumajdad, M. Madkour, Y. Abdel-Moneam and M. El-Kemary, *J. Mater. Sci.*, 2014, **49**, 1743–1754.
12 F. Azeez, E. Al-Hetlani, M. Arafa, Y. Abdelmonem, A. A. Nazeer, M. O. Amin and M. Madkour, *Sci. Rep.*, 2018, **8**, 7104.
13 K. K. Jha, A. Samad, Y. Kumar, M. Shaharyar, R. L. Khosa, J. Jain, V. Kumar and P. Singh, *Eur. J. Med. Chem.*, 2010, **45**, 4963–4967.
14 F. B. Tamboura, O. Diouf, A. H. Barry, M. Gaye and A. S. Sall, *Polyhedron*, 2012, **43**, 97–103.
15 Y. K. Abdel-Monem, S. A. Abou El-Enein and M. M. El-Sheikh-Amer, *J. Mol. Struct.*, 2017, **1127**, 386–396.
16 S. M. Emam, S. A. Abouel-Enein and E. M. Abdel-Satar, *Appl. Organomet. Chem.*, 2019, **33**, e4847.
17 S. A. Abouel-Enein, S. M. Emam and E. Monir, *Appl. Organomet. Chem.*, 2018, **32**, e4191.
18 S. Alghool, M. S. Zoromba and H. F. A. El-Halim, *J. Rare Earths*, 2013, **31**, 715–721.
19 A. K. El-Sawaf, M. A. Azzam, A. M. Abdou and E. H. Anouar, *Inorg. Chim. Acta*, 2018, **483**, 116–128.
20 M. Uma, N. Balaram, P. R. Sekhar Reddy, V. Janardhanam, V. Rajagopal Reddy, H.-J. Yun, S.-N. Lee and C.-J. Choi, *J. Electron. Mater.*, 2019, **48**, 4217–4225.
21 M. Zhang, Y. Yan, W. Han, X. Li, Z. Hou, Y. Tian, K. Ye, L. Bao, X. Li and Z. Zhang, *RSC Adv.*, 2012, **2**, 1585–1591.
22 S. Zinatloo-Ajabshir, S. Mortazavi-Derazkola and M. Salavati-Niasari, *Int. J. Hydrogen Energy*, 2017, **42**, 15178–15188.
23 A. Kumar, J. C. G. E. da Silva, K. Kumar, H. C. Swart, S. K. Maurya, P. Kumar and S. P. Tiwari, *Mater. Res. Bull.*, 2019, **112**, 28–37.
24 A. A. Ali, A. A. Nazeer, M. Madkour, A. Bumajdad and F. Al Sagheer, *Arabian J. Chem.*, 2018, **11**, 692–699.